AIAA 81-1203R

Computation of Inviscid Flow Over Blunt Bodies Having Large Embedded Subsonic Regions

K. James Weilmuenster* and H. Harris Hamilton II†
NASA Langley Research Center, Hampton, Virginia

A computer program, HALIS, designed to compute the inviscid flowfield about complex three-dimensional bodies at high angles of attack is described. The HALIS code is shown to accurately define the flowfield about both simple and complex three-dimensional geometries through comparison with experimental data and established numerical procedures. Results of computations of the flowfield about a modified Space Shuttle Orbiter are presented. These solutions cover the first 383 in. of the vehicle for angles of attack of 25-45 deg. Analysis of these computational results shows that the subsonic region on the Shuttle windward surface can be extensive at high angles of attack.

Introduction

ADVANCES in computational techniques and computers in the past few years make it practical to compute the steady inviscid flowfield about complex three-dimensional bodies, such as the Space Shuttle Orbiter or other advanced entry vehicles, in their actual supersonic or hypersonic flight environment. The inviscid flowfield provides surface pressures, which can be integrated to obtain aerodynamic loads, and other flow properties which are required to calculate surface heating rates[1] needed to define the thermal environment.

These vehicles enter the atmosphere at relatively large angles of attack, which will lead to one of two classes of problems (see Fig. 1). If the angle of attack is moderate (25-30 deg or less), the subsonic portion of the flowfield is generally confined to the vehicle nose. Several papers[2-5] have presented time-asymptotic methods for efficiently solving the three-dimensional inviscid flow over blunt-nosed bodies at moderate angles of attack where the subsonic region is relatively small. These solutions provide a data surface, downstream of the subsonic region, on which the local flow velocity is supersonic. Several papers[6-9] have presented methods for continuing the solution downstream in the supersonic region using spatial marching techniques. Since these techniques use spatial marching, they require relatively low computer storage. These methods have been shown to provide good results unless additional embedded pockets of subsonic flow are encountered (such as near the leading edge of wings) where the spatial marching techniques break down.

When the angle of attack is large (in the range 30-45 deg or higher), the subsonic region is no longer confined to the nose, but extends much further downstream and can envelop much of the lower surface (see Fig. 1). Since the entire subsonic region must be computed simultaneously, the time-asymptotic portion of the solution will require many more grid points than for the moderate angle-of-attack case discussed previously. Therefore codes must be structured for computers that have the storage and computational speed required to solve this type of problem (which may require between 25,000 and 90,000 grid points). Thus existing time-asymptotic methods[2-5] are not suited to solve the flow over complete vehicles with complex three-dimensional geometries at high angle of attack. In Ref. 10, it is shown that a vector-processing computer is ideally suited for solving this type of large flowfield problem.

This paper presents a time-asymptotic method that is being developed for the CDC Cyber 203 vector-processing computer which will be able to solve the flow over complex three-dimensional bodies (Shuttle-like geometries at large angles of attack) where large embedded subsonic regions occur. Results are presented in this paper which demonstrate the capability of the high alpha inviscid solution code, HALIS, to compute the flowfield over relatively simple geometries with large embedded subsonic regions and over the Space Shuttle Orbiter at large angles of attack.

Coordinate Systems

The solution technique used in this paper requires that all coordinate lines extending from the body to the shock originate at a point on the body, and terminate at a point on the bow shock. When treating short blunt bodies, a spherical coordinate system naturally satisfies these requirements. However, when a body becomes many nose radii long, that region of the flowfield downstream of the nose cap is better described in a cylindrical coordinate system. Thus a combined spherical-cylindrical coordinate system, as shown in Fig. 2, is used. In this right-handed system, the spherical and cylindrical coordinate systems are coupled at the $\theta = \Pi/2$, $z = 0$ plane where the two systems are coincident. Computations will be carried out in the spherical domain over

$$r_{\text{body}} \le r \le r_{\text{shock}} \qquad -\Pi/2 \le \phi \le \Pi/2 \qquad \Pi \ge \theta \ge \Pi/2$$

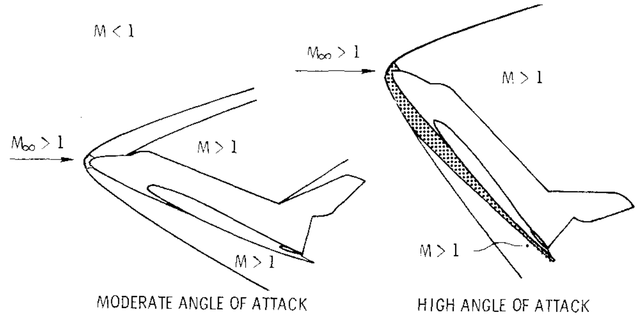

Fig. 1 External flowfields, super/hypersonic flight regime.

Presented as Paper 81-1203 at the AIAA 14th Fluid and Plasma Dynamics Conference, Palo Alto, Calif., June 23-25, 1981; submitted July 13, 1981; revision received Dec. 14, 1981. This paper is declared a work of the U.S. Government and therefore is in the public domain.

*Aero-Space Technologist, Aerothermodynamics Branch, Space Systems Division.
†Research Leader, Aerothermodynamics Branch, Space Systems Division.

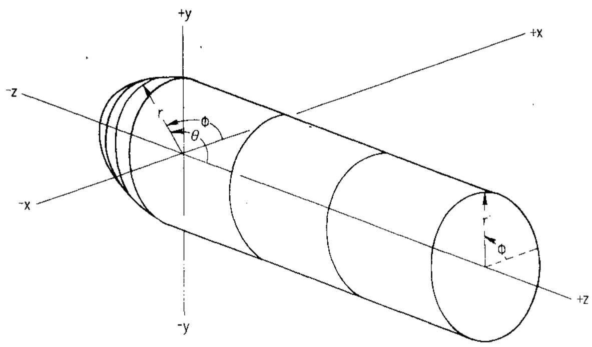

Fig. 2 Physical coordinate system.

and in the cylindrical domain over

$$r_{\text{body}} \leq r \leq r_{\text{shock}} \qquad -\Pi/2 \leq \phi \leq \Pi/2 \qquad 0 < z \leq z_{\max}$$

A typical representation of the physical grid system is shown in Fig. 3a, a symmetry plane view, and in Fig. 3b, a cross-flow plane view which corresponds to the exit plane of Fig. 3a. To improve the clarity of these two figures, a number of grid lines have been removed. As can be seen from the figures, the coordinate system in the physical domain is a skewed, nonorthogonal system.

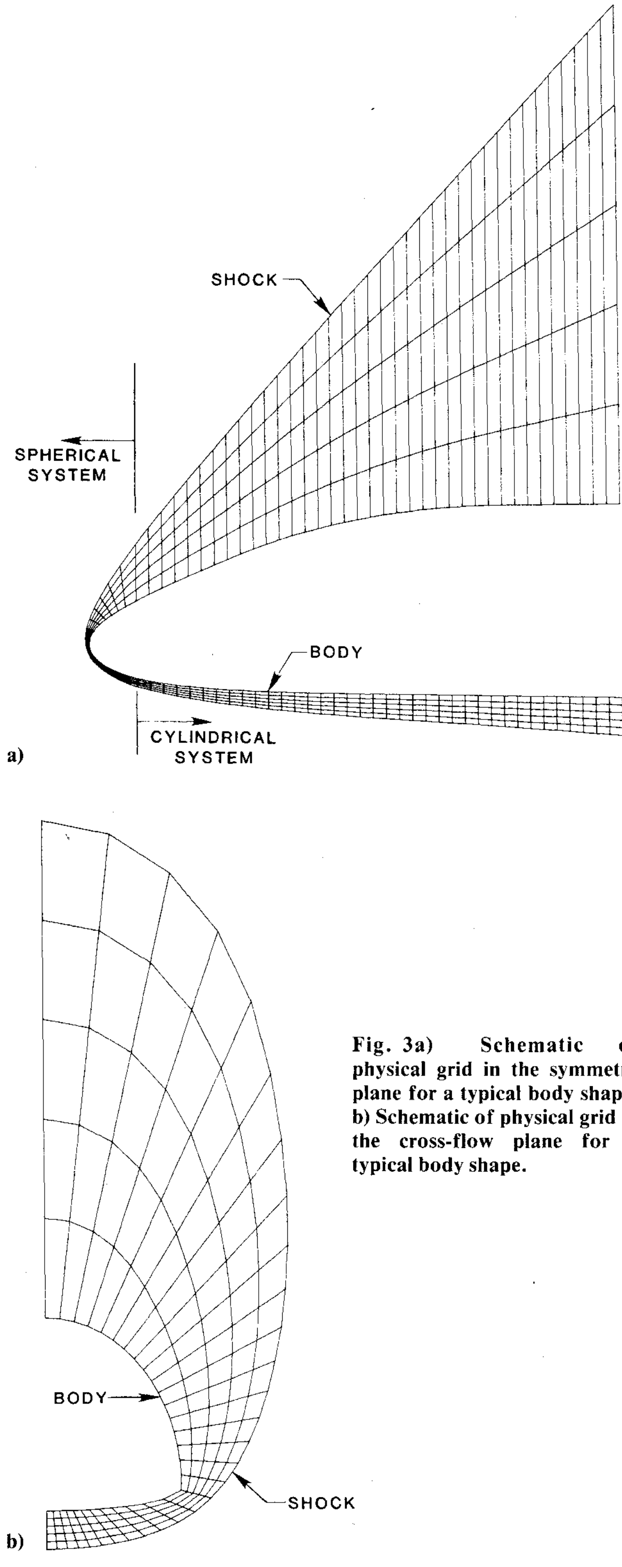

Fig. 3a) Schematic of physical grid in the symmetry plane for a typical body shape; b) Schematic of physical grid in the cross-flow plane for a typical body shape.

Method of Solution

Flow Equations

To better utilize the vector-processing characteristics of the CDC Cyber 203 computer, flowfields are determined by solving the time-dependent, three-dimensional, compressible Euler equations in conservation form as follows:

$$\frac{\partial W}{\partial t} + \frac{\partial F}{\partial x_1} + \frac{\partial H}{\partial x_2} + \frac{\partial G}{\partial x_3} + Q = 0 \tag{1}$$

The equations have been written in conservation form so that embedded shock waves can be captured. The vectors $\boldsymbol{W}, \boldsymbol{F}, \boldsymbol{H}$, and $\boldsymbol{G}$ represent the usual conserved quantities in the (x_1,x_2,x_3) coordinate system and the vector $\boldsymbol{Q}$ contains all terms that arise from the use of a non-Cartesian system. A general form of the three-dimensional Navier-Stokes equations may be found in Appendix A of Ref. 11. The form of the vectors $\boldsymbol{W}, \boldsymbol{F}, \boldsymbol{G}, \boldsymbol{H}$, and $\boldsymbol{Q}$ in both the spherical and cylindrical coordinate systems can be determined from those equations by deleting the viscous terms and substituting the appropriate metric coefficients and coordinates.

In the spherical system, the flow equations must be solved along the negative z axis which corresponds to $\theta = \Pi$ for all values of ϕ and r. Along this line, Eq. (1) does not hold because of a singularity. A reduced set of equations, valid only along the negative z axis, have been derived and are used in all computations here.

Transformations

The physical domain is transformed into two separate computational cubes, one corresponding to each coordinate system, by the following equations, which allow the description of a general body in terms of its radius. For the spherical system

$$\eta = \frac{r - r_{\text{body}}(\phi,\theta)}{r_{\text{shock}}(t,\phi,\theta) - r_{\text{body}}(\phi,\theta)} \qquad 0 \leq \eta \leq 1$$

$$\psi = \frac{\phi + \Pi/2}{\Pi} \qquad 0 \leq \psi \leq 1$$

$$\omega = \frac{\Pi - \theta}{\Pi/2} \qquad 0 \leq \omega \leq 1 \tag{2}$$

and for the cylindrical system

$$\eta = \frac{r - r_{\text{body}}(\phi,z)}{r_{\text{shock}}(t,\phi,z) - r_{\text{body}}(\phi,z)} \qquad 0 \leq \eta \leq 1$$

$$\psi = \frac{\phi + \Pi/2}{\Pi} \qquad 0 \leq \psi \leq 1$$

$$\xi = \frac{z}{z_{\max}} \qquad 0 \leq \xi \leq 1 \tag{3}$$

In Eq. (1), the partial derivatives with respect to time and the physical coordinates are replaced by the partial derivatives with respect to the computational time and coordinate space by applying chain-rule differentiation to Eqs. (2) and (3).

Although the physical mesh is transformed to a computational mesh, the velocity components are not transformed and retain the same magnitude and direction in the computational mesh as they do in the physical grid.

Boundary Conditions

For inviscid flow, the wall-boundary condition requires that the velocity component normal to the wall be zero. Since, in general, the physical grid will not be normal to the wall, nor will the cross flow and axial components of velocity be parallel to the body surface, the cross flow and axial components of velocity at the surface are computed and the radial component of velocity is set such that the condition $\boldsymbol{V}\cdot\hat{n}=0$ is satisfied. Here, $\boldsymbol{V}$ is the total velocity at the wall and $\hat{n}$ is the outer unit normal at the wall. In addition, the body surface entropy is held constant and the computed wall density, along with this entropy, are used to determine the surface internal energy and pressure.

The bow shock, which is the outer boundary of the flowfield, is a time-dependent boundary condition, since the postshock properties and shock location are a function of the computational time increment. The procedure for handling the time-dependent shock is an extension to three dimensions of the method outlined in Ref. 12. Briefly, the postshock properties are determined by the postshock pressure and the local inclination of the shock to the freestream velocity vector. The postshock pressure is taken to be the pressure at the shock location determined by the integration of the flowfield equations. From this pressure and the shock geometry, new postshock conditions and a shock velocity can be determined. The position of the shock is then updated using the computed shock speed and the local incremental time step. At convergence, the computed postshock pressure will give a zero shock velocity and thus a stationary shock wave.

Calculations in the computational plane corresponding to the ray $\theta=\Pi$ are made along the line $\phi=-\Pi/2$. Flow properties for other values of ϕ are determined from algebraic relations similar to those found in Ref. 13. The $\phi=\Pi/2$ and $\phi=-\Pi/2$ meridional planes are symmetry boundaries. Flow properties in these meridional planes are computed using a regular interior point differencing and planes of reflected properties at $\phi=\Pi/2+\Delta\phi$ and $\phi=-\Pi/2-\Delta\phi$. Flow properties in the outflow plane, where the axial flow must be supersonic, are computed using two point backward differences for the axial derivatives.

Numerical Procedure

The computational data base is arranged as shown in Fig. 4. Each plane has 11 points in the η direction (distance between shock and body) and 50 points in the ψ (meridional) direction. There are 55 planes in the streamwise direction with the first 15 being in the spherical system. This computational grid of 30,250 points along with the associated computer code requires all of the Cyber 203 central memory of 10^6 words. However, the data base is arranged in an interleaved[14] manner to make efficient use of the system's virtual memory system, should the size of the code ever exceed the available central memory.

Equation (1) is integrated in time using an unsplit MacCormack differencing scheme. Additional numerical dissipation has been added to the numerical scheme by using the fourth-order damping terms suggested by Barnwell.[13] In the predictor step, computations are carried out by sweeping through the data from left to right (see Fig. 4) and in the corrector step, by sweeping through the data from right to left to remain consistent with the interleaving concept. Rather than run the solution at one global time step, each grid point is allowed to proceed at its own local time increment as determined by the CFL condition. This same procedure was used in Ref. 11.

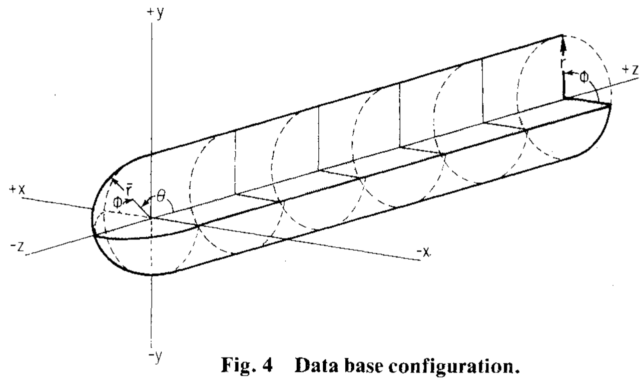

Fig. 4 Data base configuration.

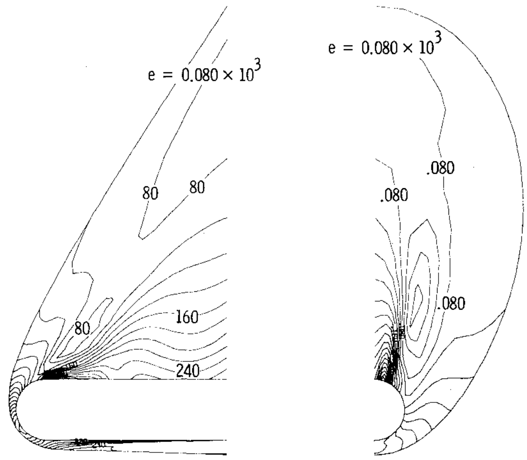

Fig. 5 Profile and cross-flow contour plots of internal energy for flow about a hemisphere cylinder at 40-deg angle of attack; $M_\infty=5$.

The solution at the plane at which the spherical and cylindrical systems are coincident ($\theta=\Pi/2$ or $Z=0$) is determined in the spherical system. This requires that data, in a spherical system that has been extended into the cylindrical domain, must be determined by interpolation on data in the cylindrical system. This procedure works well and causes no apparent numerical problem.

The number of iterations required to obtain converged solutions varies from about 450 for small angle of attack to about 1800 for very high angle of attack and seems to have little dependence on the body shape being considered. This amount of computational work translates into approximately 10-30 min of CPU time on the CDC Cyber 203 computer. A solution is considered to be converged when the relative change in the density at every point in the flowfield is less than 1.0×10^{-4}.

Results and Discussion

Initial computations were made of flow over a hemisphere cylinder. For these computations, the hemisphere was described in the spherical system and the cylinder in the cylindrical system. Figure 5 shows some results of those calculations in the form of contour plots of internal energy for a $\gamma=1.4$, $M_\infty=5$ flow at 40-deg angle of attack. In the profile view, the shock shape, as well as the contours, is seen to be smooth in the vicinity of the juncture of the two coordinate systems. Also, on the leeside of the body, the distance between the shock and body increases rapidly with increased axial distance. Since the number of points between the shock and body is fixed, the resolution of the flow in the r direction on the leeside is greatly reduced. However, this does

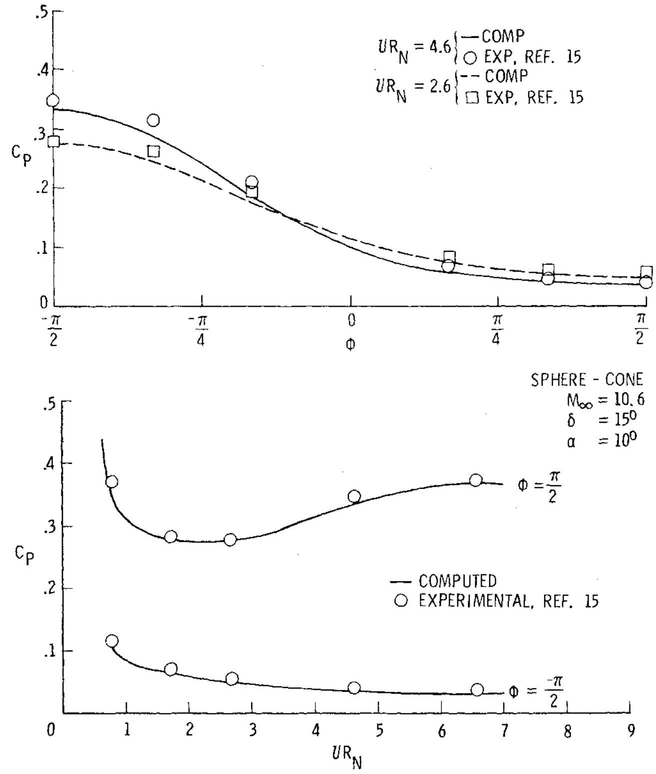

Fig. 6a) Computed and experimental windward and leeward symmetry plane wall pressure coefficient distributions for a 15-deg half-angle sphere cone at 10-deg angle of attack; $M_\infty = 10.6$. b) Computed and experimental meridional pressure coefficient distributions for a 15-deg half-angle sphere cone at 10-deg angle of attack.

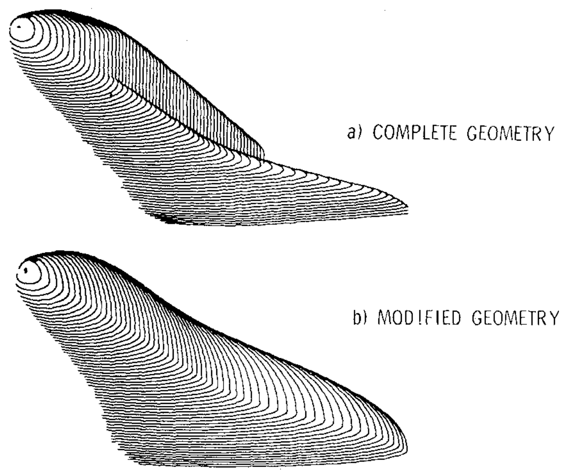

Fig. 7 Complete and modified Shuttle Orbiter geometry.

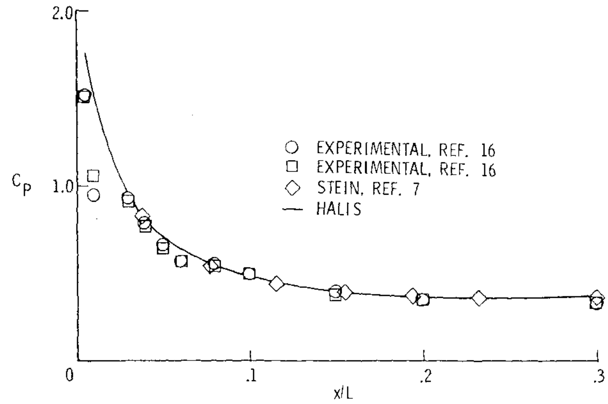

Fig. 8 Windward centerline pressure coefficient vs X/L; $\alpha = 25$ deg, $M_\infty = 10.29$.

not appear to adversely affect the computations, as can be seen in the cross-flow contour plot where a fairly strong cross-flow shock, located near the leeside symmetry plane, has been captured by the conservative equations, and where the bow shock shape is smooth in the cross section.

Further computations have been made for flow over a 15-deg half-angle sphere cone. For this body, the point of curvature discontinuity on the body surface lies in the spherical coordinate system rather than at the juncture of the two coordinate systems, as was the case for the hemisphere-cylinder body. In Fig. 6a, a comparison is made for this body between the computed windward and leeward wall pressure coefficient distributions and the experimental data of Cleary[15] for $\gamma = 1.4$, $M_\infty = 10.6$ flow at 10-deg angle of attack. As can be seen, the comparison is quite good. For this same case, Fig. 6b shows a comparison of the computed and experimental wall pressure coefficients in cross-sectional planes at two axial stations.

For both the hemisphere-cylinder and sphere-cone geometries, the subsonic flow regime is confined to the spherical nose cap even at the angle of attack considered. How the subsonic region will behave on a body whose curvature changes continuously from nose to trailing edge is of further interest. Specifically, how will the subsonic region behave on the windward side of the Space Shuttle Orbiter?

Two versions of the Space Shuttle Orbiter geometry are shown in Fig. 7. The first conforms as closely as possible to the actual vehicle except that the canopy and the tail section have been eliminated. The second geometry has the same lower surface and upper-symmetry plane profile as the first, except that the area between strake and wingtips and upper-symmetry plane surface has been filled in with elliptic curve segments. Since the windward flowfield is of specific interest, the simplified Shuttle geometry has been utilized in the following analysis.

To further validate the HALIS code, for the case of complex three-dimensional shapes, the flow about the modified Shuttle vehicle has been computed at an angle of attack for which both experimental data and numerical results are available. The numerical results were generated by STEIN,[7] a spatial marching code, while the experimental data[16] were obtained in the NASA Ames Research Center 3.5-ft Hypersonic Wind Tunnel. Figure 8 shows a comparison of numerical and experimental surface pressure coefficients on the windward centerline plotted against nondimensional body length for a 25-deg angle of attack and $M_\infty = 10.29$. The comparison among all four sets of data is excellent. In fact, the two numerical methods give almost identical results. This is interesting since both methods have the same resolution in the radial and meridional directions but the STEIN code has an axial resolution eight times greater than the HALIS code. A further comparison of the experimental and numerical results for this case is shown in Fig. 9 where meridional distributions of surface pressure coefficients are plotted for three different axial locations on the vehicle. The numerical data are plotted to approximately the tip of the vehicle strake. There is good agreement between experimental data and both sets of numerical results for off-axis points on the windward surface of the body. In Fig. 10 is shown the results for a 45-deg angle-of-attack case which could not be run using the STEIN code. Again, M_∞ is 10.29. The windward centerline surface pressure coefficient is plotted against nondimensional body length. Again, there is excellent agreement between the experimental and numerical results. In Fig. 11, the meridional surface pressure coefficient distributions are shown. Here, the comparisons are similar to those presented for the 25-deg

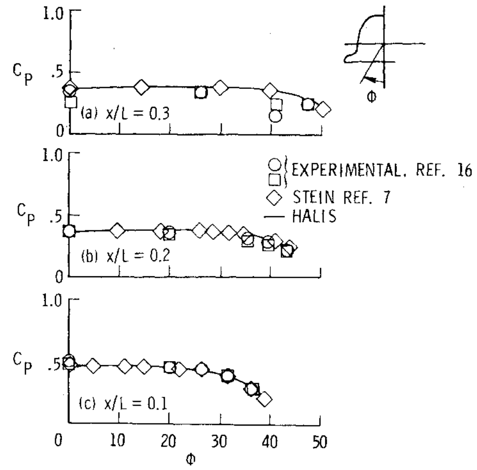

Fig. 9 Computed and experimental meridional pressure coefficient distributions; $\alpha = 25$ deg, $M_\infty = 10.29$.

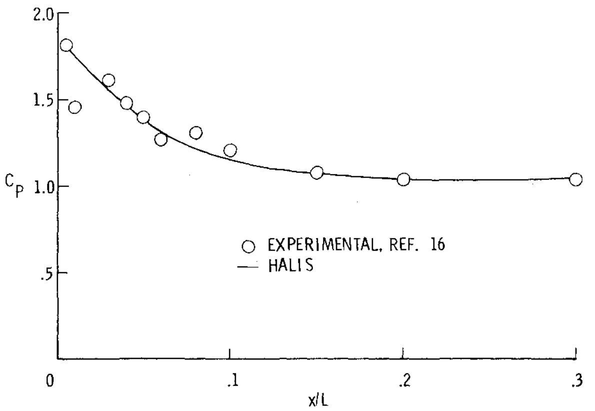

Fig. 10 Windward centerline pressure coefficient vs X/L; $\alpha = 45$ deg, $M_\infty = 10.29$.

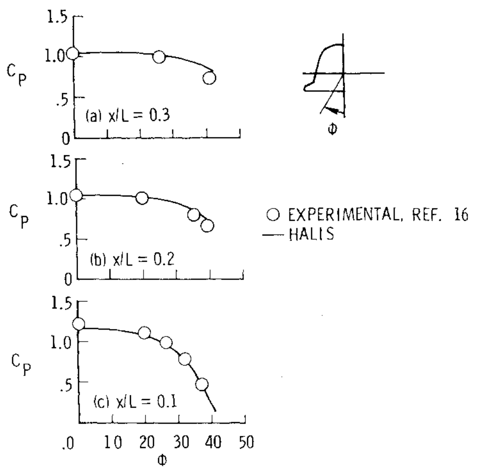

Fig. 11 Computed and experimental meridional pressure coefficient distributions; $\alpha = 45$ deg, $M_\infty = 10.29$.

angle-of attack case. Thus the validity of the HALIS codes has been established over a wide range of angle of attack.

Figures 12 and 13 show cross-sectional contour plots of internal energy 383 in. down the vehicle for a M_∞ of 7.32 and angles of attack of 25 and 45 deg. For both cases, a smooth shock shape is maintained in the leeside region where the resolution is very poor. Also, note that the leeside cross-flow shock strengthens as the angle of attack increases.

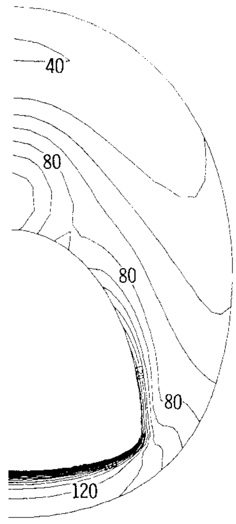

Fig. 12 Cross-section contour plot of internal energy; $Z = 383$ in., $\alpha = 25$ deg, $M_\infty = 7.32$.

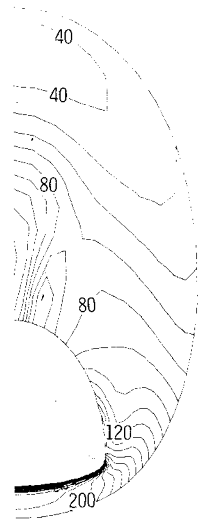

Fig. 13 Cross-section contour plot of internal energy; $Z = 383$ in., $\alpha = 40$ deg, $M_\infty = 7.32$.

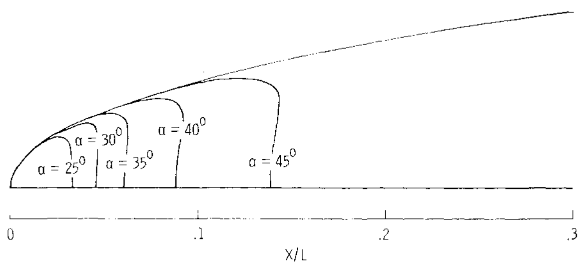

Fig. 14 Computed sonic line locations on the windward body surface for several angles of attack, $M_\infty = 7.32$.

In Fig. 14, sonic line contours are plotted as a function of angle of attack on a planform view of the windward side of the vehicle. It is immediately obvious that the area covered by the subsonic flow is changing at an increasing rate as the angle of attack is increased. In fact, the axial Mach number gradient along the surface is very small. Thus any further increases in angle of attack will lead to a very large subsonic region on the windward surface.

Conclusions

In this work, a computer code, HALIS, designed to compute the inviscid flowfield about complex three-dimensional bodies at high angle of attack has been described. Through comparison with experimental data and established numerical procedures, it has been demonstrated that the

HALIS code accurately defines the flowfield about both simple and complex three-dimensional geometries. Results have been presented of computations to determine the flowfield about a modified Space Shuttle Orbiter. These solutions encompass the first 383 in. of the vehicle and include angles of attack from 25 to 45 deg and show that, at high angles of attack, the subsonic region on the Shuttle windward surface can be extensive.

References

[1]Hamilton, H.H. II, "Calculation of Laminar Heating Rates on Three-Dimensional Configurations Using the Axisymmetric Analogue," NASA TP 1698, 1980.

[2]Moretti, G. and Bleich, G., "Three-Dimensional Flow Around Blunt Bodies," *AIAA Journal,* Vol. 5, Sept. 1967, pp. 1557-1562.

[3]Rizzi, A.W. and Inouye, M., "Time-Split Finite Volume Method for Three-Dimensional Blunt-Body Flow," *AIAA Journal,* Vol. 11, Nov. 1973, pp. 1478-1485.

[4]Hall, D.W., "Calculation of Inviscid Supersonic Flow Over Ablated Nosetips," AIAA Paper 79-342, Jan. 1979.

[5]Pulliam, T.H. and Steger, J.L., "Implicit Finite-Difference Simulations of Three-Dimensional Compressible Flow," *AIAA Journal,* Vol. 18, Feb. 1980, pp. 159-167.

[6]Marconi, F. and Salas, M., "Computation of Three-Dimensional Flows About Aircraft Configurations," *Computers and Fluids,* Vol. 1, 1973, pp. 185-195.

[7]Marconi, F., Yeager, L., and Hamilton, H.H. II, "Computation of High-Speed Inviscid Flows About Real Configurations, Aerodynamic Analysis Required Advanced Computers—Part II," NASA SP-346, 1975, pp. 1411-1435.

[8]Kutler, P., Reinhardt, W.A., and Warming, R.F., "Multishocked Three-Dimensional Supersonic Flow Fields With Real Gas Effects," *AIAA Journal,* Vol. 11, May 1973, pp. 657-664.

[9]Rizzi, A.W., Klavins, A., and MacCormack, R.W., "A Generalized Hyperbolic Marching Technique for Three-Dimensional Supersonic Flow With Shocks," paper presented at the Fourth International Conference on Numerical Methods in Fluid Dynamics, Boulder, Colo., June 1974.

[10]Weilmuenster, K.J. and Howser, L.M., "Solution of a Large Hydrodynamic Problem Using the STAR-100 Computer," NASA TM X-73904, 1976.

[11]Weilmuenster, K.J. and Hamilton, H.H. II, "A Hybridized Method for Computing High-Reynolds-Number Hypersonic Flow About Blunt Bodies," NASA TP 1497, 1979.

[12]Tannehill, J.C. and Holst, T.L., "Numerical Computation of Two-Dimensional Viscous Blunt Body Flows With an Impinging Shock," NASA CR-138594, 1974.

[13]Barnwell, R.W., "A Time-Dependent Method for Calculating Supersonic Angle-of-Attack Flow About Axisymmetric Blunt Bodies With Sharp Shoulders and Smooth Nonaxisymmetric Blunt Bodies," NASA TN D-6283, 1971.

[14]Lambiotte, J.J. Jr., "Effect of Virtual Memory on Efficient Solution of Two Model Problems," NASA TM X-3512, 1977.

[15]Cleary, J.W., "An Experimental and Theoretical Investigation of the Pressure Distribution and Flow Fields of Blunted Cones at Hypersonic Mach Numbers," NASA TN D-2969, 1965.

[16]Dye, W.H. and Polek, T., "Results of Pressure Distribution Tests of a 0.010-Scale Space Shuttle Orbiter (61-0) in the NASA/ARC 3.5-Foot Hypersonic Wind Tunnel (Test OH38)," NASA CR-144, 584, 1975.